

## Ultrastrong medium-entropy single-phase alloys designed via severe lattice distortion

Sohn, Seok Su; Kwiatkowski da Silva, Alisson; Ikeda, Yuji; Körmann, Fritz; Lu, Wenjun; Choi, Won Seok; Gault, Baptiste; Ponge, Dirk; Neugebauer, Jörg; Raabe, Dierk

**DOI**

[10.1002/adma.201807142](https://doi.org/10.1002/adma.201807142)

**Publication date**

2019

**Document Version**

Final published version

**Published in**

Advanced Materials

**Citation (APA)**

Sohn, S. S., Kwiatkowski da Silva, A., Ikeda, Y., Körmann, F., Lu, W., Choi, W. S., Gault, B., Ponge, D., Neugebauer, J., & Raabe, D. (2019). Ultrastrong medium-entropy single-phase alloys designed via severe lattice distortion. *Advanced Materials*, 31(8), [1807142]. <https://doi.org/10.1002/adma.201807142>

**Important note**

To cite this publication, please use the final published version (if applicable).  
Please check the document version above.

**Copyright**

Other than for strictly personal use, it is not permitted to download, forward or distribute the text or part of it, without the consent of the author(s) and/or copyright holder(s), unless the work is under an open content license such as Creative Commons.

**Takedown policy**

Please contact us and provide details if you believe this document breaches copyrights.  
We will remove access to the work immediately and investigate your claim.

***Green Open Access added to TU Delft Institutional Repository***

***'You share, we take care!' - Taverne project***

**<https://www.openaccess.nl/en/you-share-we-take-care>**

Otherwise as indicated in the copyright section: the publisher is the copyright holder of this work and the author uses the Dutch legislation to make this work public.

# Ultrastrong Medium-Entropy Single-Phase Alloys Designed via Severe Lattice Distortion

Seok Su Sohn,\* Alisson Kwiatkowski da Silva, Yuji Ikeda, Fritz Körmann, Wenjun Lu, Won Seok Choi, Baptiste Gault, Dirk Ponge, Jörg Neugebauer, and Dierk Raabe

Severe lattice distortion is a core effect in the design of multiprincipal element alloys with the aim to enhance yield strength, a key indicator in structural engineering. Yet, the yield strength values of medium- and high-entropy alloys investigated so far do not substantially exceed those of conventional alloys owing to the insufficient utilization of lattice distortion. Here it is shown that a simple VCoNi equiatomic medium-entropy alloy exhibits a near 1 GPa yield strength and good ductility, outperforming conventional solid-solution alloys. It is demonstrated that a wide fluctuation of the atomic bond distances in such alloys, i.e., severe lattice distortion, improves both yield stress and its sensitivity to grain size. In addition, the dislocation-mediated plasticity effectively enhances the strength–ductility relationship by generating nanosized dislocation substructures due to massive pinning. The results demonstrate that severe lattice distortion is a key property for identifying extra-strong materials for structural engineering applications.

Solving the strength–ductility trade-off dilemma is an essential challenge in advanced materials science and engineering.<sup>[1–7]</sup> Many research directions are pursued to improve the balance of strength and ductility via exploring so far unrevealed or untapped mechanisms and correspondingly controlling the microstructure.<sup>[1–9]</sup> In engineering structures, however, yield strength is an essential bound which limits the maximum stress that can be carried by a material without causing inelastic deformation.<sup>[10,11]</sup> To improve yield strength, conventional alloys usually rely on complex and expensive

thermomechanical processing routes which introduce high densities of dislocations and interfaces into materials. These defect populations introduce long-range stress fields, enabling substantial strengthening of materials. Thus, processing with the aim to introduce high densities of lattice defects into materials is a well-established and efficient method to enhance their strength.<sup>[12]</sup> Yet, when single-phase metallic materials have few defects such as in the recrystallized state and at the beginning of plastic yielding, they often have insufficient intrinsic lattice friction and thus low flow stress.<sup>[13,14]</sup> The lattice friction, quantified by the Peierls stress, is a measure of the resistance that an infinite straight dislocation has to overcome when moving from one

potential valley to the next. The height of this energy barrier scales with the intrinsic atomic-scale lattice distortions and thus differs profoundly in nature from the long-range stress fields imposed by dense defect populations. In other words, the friction stress describes how severely dislocations are dragged as they move through the distorted Peierls potential landscape of massive solid solutions. In that respect, multiprincipal element solid mixtures, often termed high- or medium-entropy alloys (HEAs or MEAs), provide a very promising material design basis because each individual atom experiences a set of different neighbor atoms creating high and ubiquitous local lattice distortions and stresses.<sup>[15,16]</sup>

In that context, multiprincipal element face-centered cubic (fcc) alloys have the potential for achieving an outstanding yield strength–ductility ratio as they naturally carry high inherent lattice distortions.<sup>[15,17,18]</sup> However, two key challenges have not been addressed in this context so far. First, the yield strength is low due to the close packed fcc lattice structure.<sup>[19–21]</sup> Second, although the friction stress of these alloys is often higher than in pure metals or binary alloys, it is still usually too close to conventional structural alloys. This means that the level of lattice distortion currently exploited in most substitutional solid solution alloys does not contribute significantly to the yield strength.<sup>[20,22–28]</sup>


Here, based on a combined theoretical and experimental approach, we show that the degree of lattice distortion is indeed a key parameter in controlling strengthening mechanisms for the design of hitherto unexplored ultrastrong medium-entropy single-phase alloys. For this purpose, we exploit vanadium (V) as a very efficient element in a

Dr. S. S. Sohn, Dr. A. Kwiatkowski da Silva, Dr. Y. Ikeda, Dr. F. Körmann, Dr. W. Lu, Dr. B. Gault, Dr. D. Ponge, Prof. J. Neugebauer, Prof. D. Raabe  
Max-Planck-Institut für Eisenforschung  
Max-Planck-Straße 1, 40237 Düsseldorf, Germany  
E-mail: s.sohn@mpie.de

Dr. Y. Ikeda  
Department of Materials Science and Engineering  
Kyoto University  
Kyoto 606-8501, Japan

Dr. F. Körmann  
Department of Materials Science and Engineering  
Delft University of Technology  
Mekelweg 2, 2628 CD, Delft, The Netherlands

Dr. W. S. Choi  
Department of Materials Science and Engineering  
Korea Advanced Institute of Science and Technology  
Daejeon 34141, South Korea

 The ORCID identification number(s) for the author(s) of this article can be found under <https://doi.org/10.1002/adma.201807142>.

DOI: 10.1002/adma.201807142

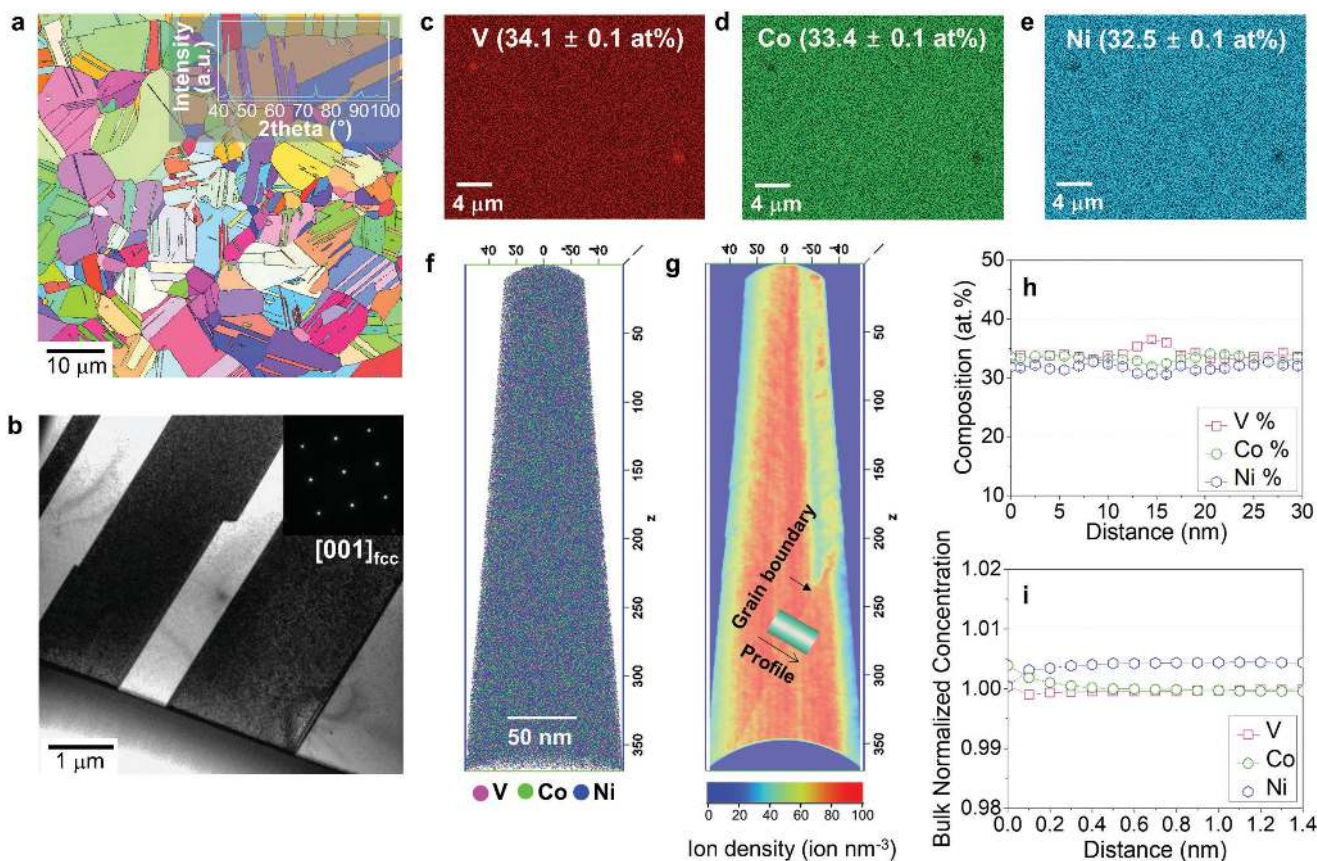


**Figure 1.** Typical microstructure of a VCoNi medium-entropy alloy. a) Electron backscatter diffraction (EBSD) inverse pole figure (IPF) map of the VCoNi alloy annealed at 900 °C for 60 min. The inset shows X-ray diffraction patterns. b) A bright-field transmission electron microscopy (TEM) image of the fcc matrix. The inset shows selected-area diffraction (SAD) patterns along the [001] zone axis of an fcc grain. c–e) Energy dispersive spectroscopy (EDS) maps of V, Co, and Ni confirming the material's chemical homogeneity. The EDS result also verifies that particles are mostly rich in V and O (Co  $19.4 \pm 1.0$  at%; Ni  $19.6 \pm 1.1$  at%; V  $34.8 \pm 0.9$  at%; O  $26.2 \pm 1.7$  at%). f) 3D atom probe tomography (APT) tip reconstructions of V, Co, and Ni atom positions. g) A 2D density map considering all detected ions. h) 1D compositional profiles (0.1 nm bin size) along the cylinder shown in g). i) Bulk normalized concentration profiles obtained by a radial distribution function analysis for V as a center ion. No chemical clustering was detected by APT analysis.

disordered VCoNi solid solution alloy. Density functional theory (DFT) simulations reveal that V significantly increases the fluctuation in the atomic bond distances, thus leading to a substantially distorted structure relative to the ideal fcc lattice. This severe lattice distortion enhances the lattice friction stress experienced by dislocations which are the main carriers of the inelastic deformation in metals. Further, as we will discuss below, it also increases the sensitivity of the yield stress on grain size changes in terms of the Hall–Petch relationship. Both, high friction stress and a high Hall–Petch coefficient significantly strengthen the current alloy. These design ideas result in a new alloy with near 1 GPa yield strength despite its precipitation-free and fully recrystallized fcc structure, i.e., strain-free grains with very low dislocation density. The alloy also shows good ductility (about 38% tensile deformation to fracture) and strain hardening capacity. The latter features arise from dislocation-mediated plasticity generating pinned nanosized dislocation substructures, thereby overcoming the so far existing strength–ductility trade-off in solid solution alloys. Our experimentally validated results demonstrate the key role of severe lattice distortions as a pertinent design

strategy for developing new alloys with high yield strength for load carrying structural applications.

The VCoNi equiatomic alloy was fabricated in a vacuum induction melting furnace under argon atmosphere. Ingots were homogenized at 1200 °C for 24 h and cold-rolled (reduction ratio; 75%) to produce 1.8 mm thick sheets. The rolled sheets were then recrystallized at 900–1200 °C for 1–60 min and immediately water-quenched. The inset in **Figure 1a** is an X-ray diffraction (XRD) pattern of the alloy annealed at 900 °C for 60 min. The alloy consists of a single fcc phase structure with a lattice parameter of 0.3601 nm. An electron backscatter diffraction (EBSD) inverse pole figure (IPF) map in **Figure 1a** shows recrystallized fcc grains with an average size of  $5.64 \pm 3.05$   $\mu\text{m}$ . The representative transmission electron microscopy (TEM) micrograph in **Figure 1b** and selected-area diffraction (SAD) patterns inset in **Figure 1b** show that the alloy is devoid of precipitates and ordered phases. The representative high-resolution high-angle annular dark-field scanning transmission electron microscopy (HAADF-STEM) micrograph and SAD patterns suggest that no precipitates or ordered phases occur at the grain boundaries (**Figure S1a**, Supporting information).

The chemical homogeneity on a microscale was observed by energy dispersive spectroscopy (EDS) (Figure 1c–e). The analysis reveals that all elements are uniformly distributed, but a few, scattered V-rich oxide particles with an average size of  $0.95 \pm 0.32 \mu\text{m}$  exist. These oxides are generally found when alloys containing reactive elements are melted and cast. It is well known that (Cr,Mn)-rich and Cr-rich oxides form in the CrMnFeCoNi high-entropy alloy<sup>[29–31]</sup> and CrCoNi medium-entropy alloy,<sup>[18,32]</sup> respectively. The average volume fraction of the V-rich oxide particles is only  $0.3 \pm 0.1\%$ , which is similar to the fraction of Cr-rich oxides reported for the CrCoNi alloy.<sup>[32]</sup> The oxide hardening contribution amounts to only 3 MPa, thus not acting as a microstructurally relevant factor for the high yield strength of the VCoNi alloy (see the Experimental Section in the Supporting Information for details). Further STEM-EDS probing (Figure S1a–d, Supporting information) also shows that there is no substantial chemical segregation of V, Co, or Ni at the grain boundaries. Atom probe tomography (APT) analysis in Figure 1f–i shows atomic-scale compositional homogeneity. The distinct high-density line feature visible in the ion density map showing the sum of all detected ions (Figure 1g) is a grain boundary. The composition profile along the cylinder across the grain boundary is shown in Figure 1h. The overall lattice composition is  $33.7 \pm 0.3$ ,  $33.4 \pm 0.4$ , and  $32.0 \pm 0.4$  (at%) for V, Co, and Ni, respectively, similar as measured by EDS. The grain boundary composition is slightly different from the grain interior with peak compositions around  $36.5 \pm 0.4$ ,  $31.9 \pm 0.4$ , and  $30.6 \pm 0.4$  (at%) for V, Co, and Ni, respectively. The segregation tendency of V can be attributed to the contribution of this element to the lattice distortion and to the consequent slight release of elastic strain energy upon segregation to regions of higher excess volume like grain boundaries.<sup>[33–35]</sup> In the investigated volume, the radial distribution function reveals no apparent local chemical ordering (Figure 1i). These results confirm that the present alloy is in a solid solution state.

Although V has been known to be prone to form intermetallic phases,<sup>[36]</sup> a disordered single solid-solution phase is maintained for the VCoNi alloy annealed at 900 °C for 60 min. This is partly from the high configuration entropy ( $\approx 1.1R$ ,  $R$ ; ideal gas constant) which enhances the stability of solid solution phases.<sup>[15]</sup> However, the configurational entropy is not the only ingredient because the mixing enthalpy, atomic size difference, and competing adjacent elemental and intermetallic phases also affect the phase stability of a solid solution.<sup>[14]</sup> Based on the Hume-Rothery rules and thermodynamic parameters to predict solid-solution phase formation in multiprincipal element alloys, the following composition-weighted terms and their empirical bounds have been developed:<sup>[37,38]</sup> i) differences in atom radii ( $\delta_r \leq 6.6\%$ ); ii) average valence electron concentration ( $\text{VEC} \geq 8$  for FCC); iii) mixing enthalpy ( $-15 \text{ kJ mol}^{-1} < \Delta H_{\text{mix}} < 5 \text{ kJ mol}^{-1}$ ); and iv) the  $\Omega$  parameter expressed by  $T_m \Delta S_{\text{mix}} / |\Delta H_{\text{mix}}|$  which combines the average melting temperature ( $T_m$ ), mixing entropy ( $\Delta S_{\text{mix}}$ ), and mixing enthalpy ( $\Omega \geq 1.1$ ). Interestingly,  $\delta_r$ , VEC,  $\Delta H_{\text{mix}}$ , and  $\Omega$  are 6.19%, 8,  $-14.2 \text{ kJ mol}^{-1}$ , and 1.22, respectively, for the current VCoNi alloy, which should indeed fulfill the empirical criteria of solid-solution phase formation.

Room-temperature stress–strain curves reveal that the VCoNi alloy has a higher strength compared to the CrCoNi alloy (389 MPa for the grain size of  $11.0 \pm 6.7 \mu\text{m}$ ) which is

known as the single fcc solid solution alloy currently exhibiting the highest yield strength in a recrystallized state (460 MPa for the grain size of  $\approx 6.5 \mu\text{m}$ ) (Figure 2a).<sup>[17,18,21,22,26]</sup> Of particular significance is that the fine-grained VCoNi alloy (grain size of  $2.0 \pm 1.5 \mu\text{m}$ ) reaches a yield strength of nearly 1 GPa despite being in a single fcc solid solution state. In addition, the alloy shows an ultimate tensile strength of 1359 MPa and a large total elongation of 38%, revealing also high strain hardening capability (Table S1, Supporting information).

Of specific interest in the field of massive solid solution alloys is the question of how severely the lattice distortions and the associated lattice friction affect the macroscopic mechanical properties. Since direct observation of single atom lattice distortion is experimentally not accessible, we reveal these effects here for the VCoNi alloy system by combining mean field experimental ab initio theoretical approaches. The lattice distortions are clearly revealed in terms of the experimentally obtained friction stresses of the materials. This approach is in line with corresponding previous studies on solid solution distortion effects in HEAs and MEAs compared to conventional alloys using friction stress measurements.<sup>[20,22–28]</sup> In addition, ab initio calculations have been recognized as a reliable method to investigate atomic scale solid solution structures and the associated local distortions.<sup>[39,40]</sup>

First, the role of the atomic scale solid solution dependent lattice distortions on the mechanical properties was studied by performing tensile tests after varying the annealing conditions and under consideration of the alloy's average grain sizes (Table S1, Supporting information). Figure 2b reveals that the yield strength and grain size well agree with a Hall–Petch strengthening behavior with an R-square of 98.6%. The measurement of the friction stress must be conducted very carefully as it is derived from the yield strength, which can actually contain various strengthening contributions in polycrystalline materials: There are first, the intrinsic friction stress (which is the main objective in the current study); second, grain-boundary strengthening (the so-called Hall–Petch effect); third, dislocation hardening (creating long-range stress fields scaling with  $\approx 1/r$ ); fourth, precipitation hardening; and fifth, oxide dispersion hardening. In the current VCoNi alloys, the latter three contributions (dislocation, precipitation, and oxide) to the yield strength are all negligible (6–14 MPa, see the Experimental Section in the Supporting Information for details) compared to the much larger contribution of the measured lattice friction stress obtained after Hall–Petch correction. This means that in the current case the corrected yield strength serves as a good measure of the lattice distortions acting in the alloy. Based on this conclusion, we compared the friction stress of the VCoNi alloy with those observed for conventional alloys.

The calculated lattice friction stress ( $\sigma_0$ ) of the VCoNi alloy is 383 MPa, which is almost three times higher than that of the previous medium- or high-entropy alloys and of conventional austenitic steels (Table S2, Supporting information).<sup>[20,22–27]</sup> Therefore, the severe lattice distortion is indeed a most effective alloy design approach for enhancing strength through an adjusted solid solution blend as demonstrated here for the VCoNi alloy. It should also be noted that the Hall–Petch coefficient of  $864 \text{ MPa } \mu\text{m}^{1/2}$  is remarkably large. This strong dependence of strength upon grain size change implies that



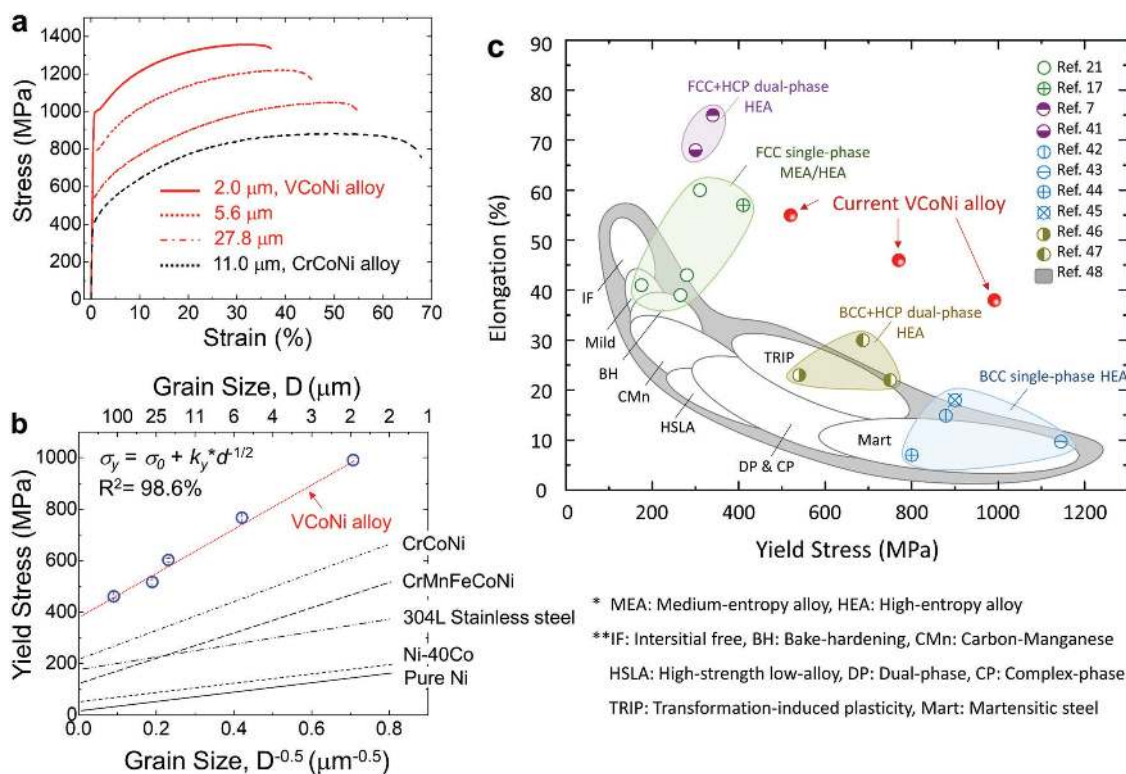


**Figure 2.** Room-temperature tensile properties of VCoNi alloys compared with selected high strength alloys. a) Engineering stress–strain curves of the annealed VCoNi and CrCoNi alloys. b) Dependence of the yield stress (measured by 0.2% offset) on the average grain size of VCoNi alloys annealed at various conditions. The dependence is compared with the reconstruction plot from the Hall–Petch coefficient ( $k_y$ ) and friction stress ( $\sigma_0$ ) of conventional alloys.<sup>[20,22–27]</sup> c) Overview of yield stress versus elongation values for the current VCoNi alloy, in relation to several high strength steels and single or multiphase high-/medium-entropy alloys. The excellent combination of strength and ductility of the VCoNi alloys surpasses that of the other high- and medium-entropy solid-solution alloys.<sup>[7,17,21,41–48]</sup>

grain refinement plays a significant role in further improving the yield strength. These notable properties are put in perspective in Figure 2c, with a direct comparison with high strength steels as well as high- and medium-entropy alloys.<sup>[7,17,21,41–48]</sup> Owing to the high friction stress, the Hall–Petch coefficient, and the high strain hardening capability, the VCoNi alloys show an excellent combination of strength and ductility surpassing that of conventional high- and medium-entropy solid-solution alloys. Note that all the investigated high- and medium-entropy alloys are in a fully recrystallized state. Tuning properties via microstructural control warrants further study in the VCoNi alloy.

To understand the origin of the high friction stress, we considered the classical theory for the lattice friction stress (i.e., Peierls stress) which can be expressed using the following Equation (1)<sup>[49,50]</sup>

$$\sigma_0 = 2MG/(1-\nu) \cdot \exp(-2\pi w/b) \quad (1)$$

where  $M = 3.06$  is the Taylor factor for fcc,  $G$  is the shear modulus,  $\nu$  is the Poisson's ratio,  $w$  is the width of a dislocation, and  $b$  is the magnitude of the Burgers vector. We compared the width of a dislocation normalized by the Burgers vector ( $w/b$ ) for various Ni-containing equiatomic alloys (Figure S2 and Table S3, Supporting information).<sup>[21,28,29]</sup> The  $\sigma_0$  and  $w/b$  closely follow an inverse exponential relationship. The

remarkable shrinkage of the dislocation width is observed in multiprincipal element alloys compared to pure Ni or binary Ni alloy, rendering the dislocation movement more difficult. This reduced width thus leads to the high friction stress, in agreement with the previous report.<sup>[28]</sup> Specifically, the width of a dislocation in the current VCoNi alloy presents the lowest value of 1.19 among all reported alloys. The degree of the dislocation width reduction could be a significant factor for generating the high friction stress because it represents a measure of the reduced distance over which the lattice is distorted due to the presence of a dislocation. However, a mere average value of the reduction in dislocation width does not adequately embody the nature of this effect in multiprincipal element alloys, where the lattice is no longer periodic but becomes irregular.

Our ab initio calculations further indeed reveal these atomic-scale local lattice distortion fields arising from the locally reduced symmetry. Recent studies also suggest a correlation between the degree of lattice distortions (accessible via ab initio calculations) and experimentally measured yield strengths (related to an enhanced friction stress).<sup>[39,40]</sup> The main results of our calculations are presented in Figure 3. The calculations elucidate two important contributions of V when alloyed into Co and Ni. The first observation is the change of the average atomic (Voronoi) volume of the individual elements in VCoNi and CrCoNi alloys as compared to their elemental volumes in the fcc phases (Figure 3a). Note that elemental phase data

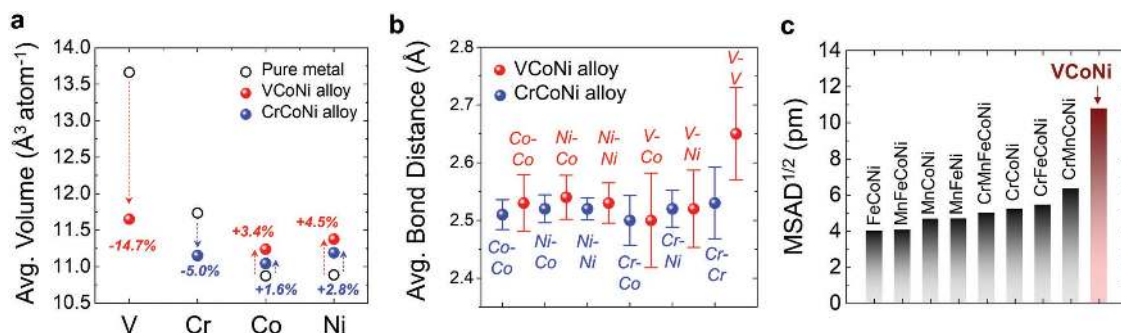


**Figure 3.** Ab initio calculations for the local lattice distortion effect. a) Relative changes of an average atomic (Voronoi) volume of the individual elements in VCoNi and CrCoNi alloys in comparison with the volumes of the pure elements in the fcc phases. Relative changes are caused not only by the alloying effect but also by macroscopic lattice constant changes between specific elements in the alloys and the corresponding elemental phases (3.575 Å for VCoNi; 3.544 Å for CrCoNi). b) First nearest-neighbor distances of each elemental pairs in the VCoNi and CrCoNi alloys. The mean value and their fluctuations were evaluated by fitting the computed bond distances to normal distribution functions (Figure S2a,b, Supporting information). c) Mean square atomic displacement (MSAD) for various multiprincipal element alloys.

pertain to the “fcc” structures and not to their respective ground-state structures. An expansion of the Co and Ni atoms and a contraction of the Cr atom can be readily expected due to their atomic size differences when rendered jointly into the solid solution lattice. V has a larger atomic size than Cr, and the relative changes of expansion and contraction in the VCoNi alloy are thus higher than those found in the CrCoNi alloy. The contraction of V is  $-14.7\%$ , which is indeed three times larger than that of Cr.

The second contribution of V is the increase of strength by introducing large fluctuations of the bond distances. An atom surrounded by atoms of a different species is subjected to lattice strain and stress because of differences in atomic size.<sup>[15]</sup> The large atomic size of V, and the associated relative larger atomic size differences in VCoNi can generate higher friction stresses when dislocations pass through the material. This is also reflected in the calculated fluctuations of the bond distances, a measure which allows more quantitative insights into the lattice distortions than the mere comparison of the mean volumes and their differences to those of the pure elements. Figure 3b shows the first nearest-neighbor distances of all elemental pair combinations in the VCoNi and CrCoNi alloys. The computed bond distances for both alloys were fitted to normal distribution functions to evaluate the mean values and their fluctuations, i.e., the standard deviations (Figure S3a,b, Supporting information). The results for CrCoNi reveal that the mean bond distances do not strongly vary among the considered pairs except for the Cr–Cr bonds, which display slightly larger bond distances (2.53 Å) as compared to the others (2.50–2.53 Å). Interestingly, the fluctuations of bond distances for Cr-containing pairs are larger than those for Co–Co, Ni–Co, and Ni–Ni pairs, a finding which has also been recently made in the CrMnFeCoNi (Cantor) alloy.<sup>[51]</sup> These larger fluctuations imply that Cr promotes local lattice distortions. In the VCoNi, the mean bond distance of the V–V pairs is apparently much larger than those of any other pair combination with a mean value of  $\approx 2.65$  Å. In addition, overall fluctuations of the bond distances even exceed those found for the CrCoNi. The lattice friction stress, also known as the Peierls–Nabarro stress, is an intrinsic obstacle that dislocations have to overcome during their movement. This stress strongly depends on the

dislocation width and Burgers vector. As a result of local lattice distortions, both should be prone to increased fluctuations resulting in a locally fluctuating Peierls potential for dislocations. This fluctuation should eventually yield increased lattice friction and friction stress.<sup>[40]</sup> Inspecting the pair-resolved bond distances, all V-containing pairs reveal large bond distance fluctuations, thus confirming the dominant role of V in generating severe local lattice distortions.

We further quantified the local lattice distortion by computing the mean square atomic displacement (MSAD, cf. Methods) (shown in Figure 3c), i.e., the deviation of the internal atomic positions from the ideal lattice sites. It has been recently shown that this quantity linearly correlates with the 0 K yield strength.<sup>[39,40]</sup> The current VCoNi alloy also well fits on the linear correlation (Figure S4, Supporting information). The MSAD value of VCoNi is almost twice as large as for the investigated ternary, quaternary, and quinary alloys in Figure 3c, further corroborating our findings of very high lattice distortions in the VCoNi alloy. This distortion leads to a lattice friction stress as calculated by the Hall–Petch relation and contributes to a potential superior mechanical performance of up to  $\approx 1$  GPa of yield strength.

However, an outstanding yield strength is attributed not only to a high friction stress, but also to grain boundary strengthening, which implies a high sensitivity of the yield stress to grain size (Table S2, Supporting information). Ever since this Hall–Petch relation was empirically introduced at first, much effort has been devoted to explaining it from a fundamental aspect of dislocation nucleation mechanism. The dislocation sources are mainly categorized as the grain-boundary ledges themselves and the grain interiors producing the stress concentration by a pile-up to the adjacent grain. Here in this study, at the onset of plastic deformation, we observed that most dislocations arise from Frank–Read dislocation sources<sup>[52]</sup> in the grain interiors for both, fine- and coarse-grained alloys (Figure S5, Supporting information). For the interior source model, the original definition of the Hall–Petch coefficient  $k_y$  reads as Equation (2)<sup>[53]</sup>

$$k_y = m^2 \tau_c r^{1/2} \quad (2)$$

where  $m$  is the orientation factor related to the orientation relative to the loading direction and to the number of activated slip systems,  $\tau_c$  stands for the critical resolved shear stress (CRSS) required for operation of a dislocation source inside a grain, and  $r$  indicates the distance of the dislocation source in the adjacent grain from the nearest dislocation pile-up in the considered grain. The dislocation density thus may control the distance  $r$  although there is still some uncertainty about the exact nature of this term  $r$ .<sup>[53]</sup>

Assuming that our current alloy and regular recrystallized fcc alloys have similar numbers of activated slip systems ( $m$ ) and source distance values ( $r$ ), the CRSS plays the most significant role for determining nucleation of dislocations. The CRSS value—except for its temperature dependence—is in solid solutions essentially determined by the Peierls stress, i.e., the minimum shear stress required to move a dislocation at 0 K against the lattice friction.<sup>[54]</sup> Thus, the high lattice friction induces high Peierls stress and high CRSS consequently, thereby leading to high  $k_y$  value. The coefficient  $k_y$  in the Hall–Petch relation is not exactly proportional to the measured lattice friction stress ( $\sigma_0$ ), but typically higher, in particular for high- or medium-entropy alloys (Figure S6 and Table S2, Supporting information). Thus, the severe lattice distortions generating the high lattice friction also enhance the sensitivity of the yield stress to grain size, i.e., grain boundary strengthening which results in 864 MPa  $\mu\text{m}^{1/2}$  for the  $k_y$  value.

To understand the high strain hardening capability and the resulting excellent combination of strength and ductility, we

performed EBSD experiments on the 40%-deformed VCoNi alloy with 5.6  $\mu\text{m}$  of grain size. Figure 4a–c shows EBSD IPF, kernel average misorientation (KAM), and image quality (IQ) maps. Neither deformation twinning nor deformation-induced phase transformation was observed during tensile straining (Figure 4a). Instead, the KAM map reveals straight and elongated strain localization features at grain boundary and also in the grain interiors. These patterns reflect modest double cross slip activity through planar dislocation cores and hence pronounced planar pile-up configurations and accumulation of geometrically necessary dislocations.<sup>[55,56]</sup> The misorientation profile, calculated through the parallel line defects in the region highlighted by the dashed white box in Figure 4c and plotted in Figure 4d, shows the generation of low-angle grain boundaries in terms of the stepwise increments of the local misorientations. This deformation substructure suggests that planar arrays of high dislocation density walls contribute to the plastic accommodation and hardening processes.

To further reveal the evolution of the deformation structure and the underlying plasticity mechanisms, we performed electron channeling contrast imaging (ECCI) analyses on the 5%, 10%, and 40%-deformed samples (Figure 4e–g). At early deformation stages, the alloy deforms by typical planar dislocation glide on  $\{111\}$  planes. Frank–Read sources indicated by white arrows and the lack of intense cross slip results in planar slip character and formation of crystallographically aligned slip bands. As the applied strain increases to 10%, dense dislocation networks start to form with activation of

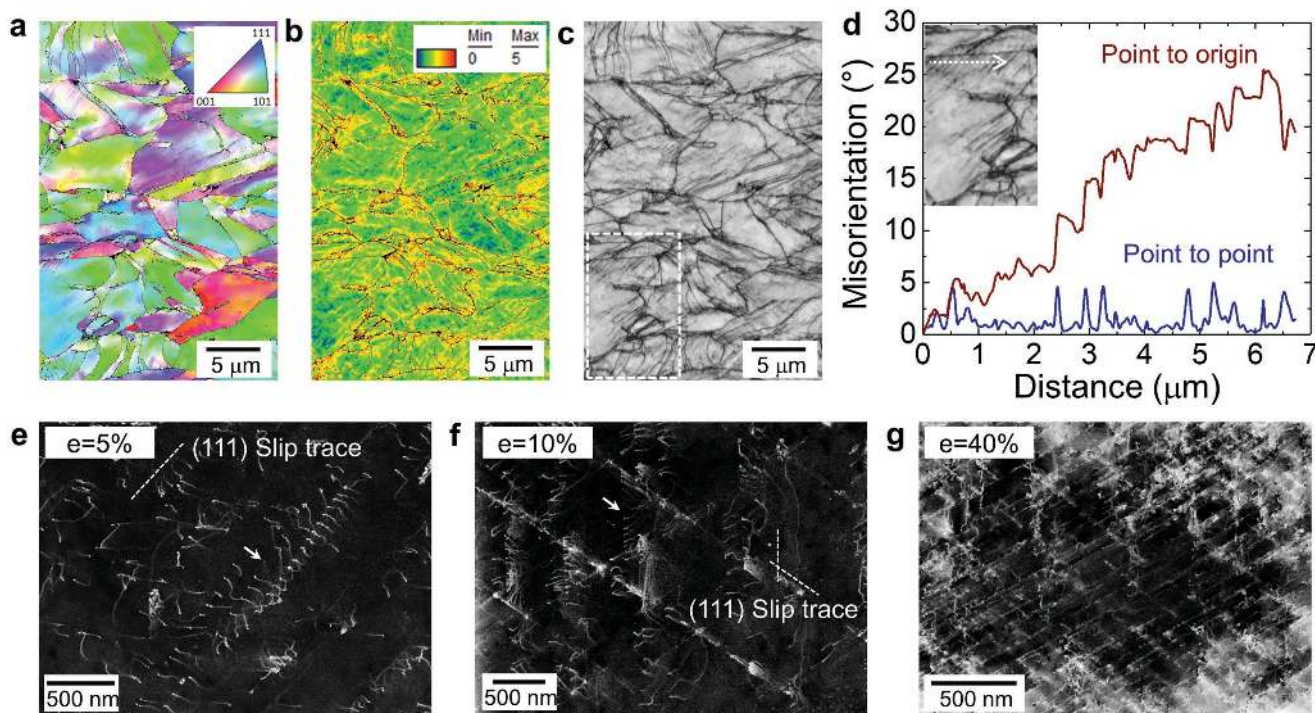


**Figure 4.** Deformation mechanisms of a VCoNi alloy. a–c) EBSD IPF, kernel average misorientation (KAM), and image quality (IQ) maps of the 40%-deformed VCoNi alloy annealed at 900 °C for 60 min devoid of any deformation twinning or deformation-induced phase transformation during tensile straining. d) The corresponding plots of the misorientation variation measured both with respect to the origin and from point to point, across a white arrow in inset area of c). e–g) Electron channeling contrast imaging (ECCI) analyses for the 5%, 10%, and 40%-deformed samples revealing the formation of nanosized planar dislocation substructures.



non-coplanar slip system with reduced slip band spacing of  $\approx 530$  nm. Upon further deformation, the spacing between coplanar slip bands is remarkably refined to  $\approx 40$  nm and slip bands intersect more frequently, creating a nanosized dislocation substructure.

The high dislocation density in the concentrated slip bands effectively reduces the mean free path of the mobile dislocations. Also, dislocation slip on parallel slip bands is increasingly impeded by the high passing stresses as the slip band spacing gets finer at higher loads (Figure 4g). The absence of frequent cross slip reduces dynamic recovery and promotes massive dislocation storage.<sup>[57]</sup> Such a mechanism of finely structured parallel slip bands with only  $\approx 40$  nm spacing at elevated loads leads to the high and sustained strain hardening rate observed in the current alloy. A similar microstructure-strain hardening relationship has been identified before for Fe-Mn-Al-C alloys as the main mechanism for high strength and good ductility.<sup>[55,56]</sup>

The lattice distortion in MEAs/HEAs was discussed quite controversially in the literature, and in most cases, it was indeed not so much larger compared to that in conventional alloys. Here, we find that the severe lattice distortion indeed substantially improves the strength through an adjusted solid solution alloying concept. Many of the recent approaches in medium- or high-entropy alloy design deviate from the original idea of single-phase stabilization for improving mechanical properties, moving toward multiphase and precipitate containing material concepts.<sup>[58]</sup> However, our results demonstrate that for a single-phase homogeneous solid solution fcc alloy, the inherent severe lattice distortions can substantially improve the friction stress enhancing both strength and its sensitivity to grain size, to eventually realize a near 1 GPa yield strength. Also, our quantum mechanical calculations elucidate the associated local distortions, enabling the quantitative visualization of the local low-symmetry structures at the atomic scale. We emphasize that these remarkable properties arise from only two kinds of fundamental strengthening mechanism, i.e., solid-solution and grain-boundary strengthening. This builds the basis for improving such alloys further, e.g., by doping them with interstitials or by introducing nanosized precipitates. Regarding the empirical criteria of solid-solution phase formation each of the parameters used in the current study is already close to their respective limits. Therefore, we envisage that the VCoNi medium-entropy alloy introduced here has the highest friction stress so far reported for any fcc solid-solution multi-principal element alloy.

## Supporting Information

Supporting Information is available from the Wiley Online Library or from the author.

## Acknowledgements

S.S.S. is grateful for the kind support of the Alexander von Humboldt Stiftung (AvH, Alexander von Humboldt Foundation, <https://www.humboldt-foundation.de>). Y.I. acknowledges the Grant-in-Aid for Scientific Research on Innovative Areas "Nano Informatics" (Grant No. 25106005) from the Japan Society for the Promotion of

Science (JSPS), the Funding by the Ministry of Education, Culture, Sports, Science and Technology (MEXT), Japan, through Elements Strategy Initiative for Structural Materials (ESISM) of Kyoto University, and the Grant-in-Aid for Young Scientist (B) of JSPS (Grant No. 16K18228). Y.I., F.K., and D.R. gratefully acknowledge funding from the Deutsche Forschungsgemeinschaft (SPP 2006). F.K. gratefully acknowledges NWO/ STW (VIDI Grant 15707). A.K.S. is grateful to the Brazilian National Research Council (Conselho Nacional de Pesquisas, CNPQ) for the PhD scholarship through the "Science without Borders" Project (203077/2014-8).

## Conflict of Interest

The authors declare no conflict of interest.

## Keywords

ab initio calculation, atomic bond distances, lattice distortion, medium-entropy alloys, tensile properties

Received: November 5, 2018

Revised: December 12, 2018

Published online: December 28, 2018

- [1] Y. Wang, M. Chen, F. Zhou, E. Ma, *Nature* **2002**, 419, 912.
- [2] Y. M. Wang, T. Voisin, J. T. McKeown, J. Ye, N. P. Clata, Z. Li, Z. Zeng, Y. Zhang, W. Chen, T. T. Roehling, R. T. Ott, M. K. Santala, P. J. Depond, M. J. Matthews, A. V. Hamza, T. Zhu, *Nat. Mater.* **2018**, 17, 63.
- [3] K. Lu, *Science* **2014**, 345, 1455.
- [4] A. Khalajehdayati, Z. Pan, T. J. Rupert, *Nat. Commun.* **2016**, 7, 10802.
- [5] Y. Wei, Y. Li, L. Zhu, Y. Liu, X. Lei, G. Wang, Y. Wu, Z. Mi, J. Liu, H. Wang, H. Gao, *Nat. Commun.* **2014**, 5, 3580.
- [6] Y. T. Zhu, X. Liao, *Nat. Mater.* **2004**, 3, 351.
- [7] Z. Li, K. G. Pradeep, Y. Deng, D. Raabe, C. C. Tasan, *Nature* **2016**, 534, 227.
- [8] T. H. Fang, W. L. Li, N. R. Tao, K. Lu, *Science* **2011**, 331, 1587.
- [9] K. Lu, L. Lu, S. Suresh, *Science* **2009**, 324, 349.
- [10] S. Jiang, H. Wang, Y. Wu, X. Liu, H. Chen, M. Yao, B. Gault, D. Ponge, D. Raabe, A. Hirata, M. Chen, Y. Wang, Z. Lu, *Nature* **2017**, 544, 460.
- [11] S.-H. Kim, H. Kim, N. J. Kim, *Nature* **2015**, 518, 77.
- [12] M. Yang, D. Yan, F. Yuan, P. Jiang, E. Ma, X. Wu, *Proc. Natl. Acad. Sci. USA* **2018**, 115, 7224.
- [13] B. B. He, B. Hu, W. H. Yen, G. J. Cheng, Z. K. Wang, H. W. Luo, M. X. Huang, *Science* **2017**, 357, 1029.
- [14] R. Valiev, *Nat. Mater.* **2004**, 3, 511.
- [15] J.-W. Yeh, *JOM* **2013**, 65, 1759.
- [16] B. Cantor, I. T. H. Chang, P. Knight, A. J. B. Vincent, *Mater. Sci. Eng., A* **2004**, 375-377, 213.
- [17] B. Gludovatz, A. Hohenwarter, D. Catoor, E. H. Chang, E. P. George, R. O. Ritchie, *Science* **2014**, 345, 1153.
- [18] B. Gludovatz, A. Hohenwarter, K. V. S. Thurston, H. Bei, Z. Wu, E. P. George, R. O. Ritchie, *Nat. Commun.* **2016**, 7, 10602.
- [19] J. B. Seol, J. W. Bae, Z. Li, J. C. Han, J. G. Kim, D. Raabe, H. S. Kim, *Acta Mater.* **2018**, 151, 366.
- [20] F. Otto, A. Dlouhý, Ch. Somsen, H. Bei, G. Eggeler, E. P. George, *Acta Mater.* **2013**, 61, 5743.
- [21] Z. Wu, H. Bei, G. M. Pharr, E. P. George, *Acta Mater.* **2014**, 81, 428.

- [22] Y. L. Zhao, T. Yang, Y. Tong, J. Wang, J. H. Luan, Z. B. Jiao, D. Chen, Y. Yang, A. Hu, C. T. Liu, J.-J. Kai, *Acta Mater.* **2017**, *138*, 72.
- [23] F. de las Cuevas, M. Reis, A. Ferraiuolo, G. Pralongo, L. P. Karjalainen, J. Alkorta, J. Gil Sevillano, *Key Eng. Mater.* **2010**, *423*, 147.
- [24] M. Odnobokova, A. Belyakov, R. Kaibyshev, *Metals* **2015**, *5*, 656.
- [25] C. Keller, E. Hug, *Mater. Lett.* **2008**, *62*, 1718.
- [26] S. Yoshida, T. Bhattacharjee, Y. Bai, N. Tsuji, *Scr. Mater.* **2017**, *134*, 33.
- [27] N. Hansen, *Acta Metall.* **1977**, *25*, 863.
- [28] Y. Y. Zhao, T. G. Nieh, *Intermetallics* **2017**, *86*, 45.
- [29] A. Gali, E. P. George, *Intermetallics* **2013**, *39*, 74.
- [30] F. Otto, N. L. Hanold, E. P. George, *Intermetallics* **2014**, *54*, 39.
- [31] E. J. Pickering, R. Muñoz-Moreno, H. J. Stone, N. G. Jones, *Scr. Mater.* **2016**, *113*, 106.
- [32] G. Laplanche, A. Kostka, C. Reinhart, J. Hunfeld, G. Eggeler, E. P. George, *Acta Mater.* **2017**, *128*, 292.
- [33] D. McLean, *Grain Boundaries in Metals*, Clarendon Press, Oxford, UK **1957**.
- [34] W. D. Kaplan, D. Chatain, P. Wynblatt, W. C. Carter, *J. Mater. Sci.* **2013**, *48*, 5681.
- [35] J. Friedel, *Adv. Phys.* **1954**, *3*, 446.
- [36] N. D. Stepanov, D. G. Shaysultanov, G. A. Salishchev, M. A. Tikhonovsky, E. E. Oleynik, A. S. Tortika, O. N. Senkov, *J. Alloys Compd.* **2015**, *628*, 170.
- [37] Y. Zhang, Y. J. Zhou, J. P. Lin, G. L. Chen, P. K. Liaw, *Adv. Eng. Mater.* **2008**, *10*, 534.
- [38] X. Yang, Y. Zhang, *Mater. Chem. Phys.* **2012**, *132*, 233.
- [39] H. S. Oh, D. Ma, G. P. Leyson, B. Grabowski, E. S. Park, F. Körmann, D. Raabe, *Entropy* **2016**, *18*, 321.
- [40] N. L. Okamoto, K. Yuge, K. Tanaka, H. Inui, E. P. George, *AIP Adv.* **2016**, *6*, 125008.
- [41] Z. Li, C. C. Tasan, K. G. Pradeep, D. Raabe, *Acta Mater.* **2017**, *131*, 323.
- [42] Y. D. Wu, Y. H. Cai, T. Wang, J. J. Si, J. Zhu, Y. D. Wang, X. D. Hui, *Mater. Lett.* **2014**, *130*, 277.
- [43] O. N. Senkov, S. L. Semiatin, *J. Alloys Compd.* **2015**, *649*, 1110.
- [44] G. Dirras, L. Liliensten, P. Djemia, M. Laurent-Brocq, D. Tingaud, J.-P. Couzinié, L. Perrière, T. Chauveau, I. Guillot, *Mater. Sci. Eng., A* **2016**, *654*, 30.
- [45] S. Sheikh, S. Shafeie, Q. Hu, J. Ahlström, C. Persson, J. Vesely, J. Zýka, U. Klement, S. Guo, *J. Appl. Phys.* **2016**, *120*, 164902.
- [46] L. Liliensten, J.-P. Couzinié, J. Bourgon, L. Perrière, G. Dirras, F. Prima, I. Guillot, *Mater. Res. Lett.* **2017**, *5*, 110.
- [47] H. Huang, Y. Wu, J. He, H. Wang, X. Liu, K. An, W. Wu, Z. Lu, *Adv. Mater.* **2017**, *29*, 1701678.
- [48] J. Liu, Y. Jin, X. Fang, C. Chen, Q. Feng, X. Liu, Y. Chen, T. Suo, F. Zhao, T. Huang, H. Wang, X. Wang, Y. Fang, Y. Wei, L. Meng, J. Lu, W. Yang, *Sci. Rep.* **2016**, *6*, 35345.
- [49] R. Peierls, *Proc. Phys. Soc.* **1940**, *52*, 34.
- [50] F. R. N. Nabarro, *Proc. Phys. Soc.* **1947**, *59*, 256.
- [51] M. Komarasamy, N. Kumar, R. S. Mishra, P. K. Liaw, *Mater. Sci. Eng., A* **2016**, *654*, 256.
- [52] J. Fisher, E. Hart, R. Pry, *Phys. Rev.* **1952**, *87*, 958.
- [53] R. Armstrong, I. Codd, R. M. Douthwaite, N. J. Petch, *Philos. Mag.* **1962**, *7*, 45.
- [54] D. Caillard, J. L. Martin, *Thermally Activated Mechanisms in Crystal Plasticity*, Elsevier, Oxford, UK **2003**.
- [55] M. J. Yao, E. Welsch, D. Ponge, S. M. H. Haghghat, S. Sandlöbes, P. Choi, M. Herbig, I. Bleskov, T. Hickel, M. Lipinska-Chwalek, P. Shanthraj, C. Scheu, S. Zaefferer, B. Gault, D. Raabe, *Acta Mater.* **2017**, *140*, 258.
- [56] E. Welsch, D. Ponge, S. M. H. Haghghat, S. Sandlöbes, P. Choi, M. Herbig, S. Zaefferer, D. Raabe, *Acta Mater.* **2016**, *116*, 188.
- [57] D. Kuhlmann-Wilsdorf, *Mater. Sci. Eng., A* **1989**, *113*, 1.
- [58] D. B. Miracle, O. N. Senkov, *Acta Mater.* **2017**, *122*, 448.